



#### **PAPER**

# Short-range-order degree dominated physical and mechanical properties of refractory multi-principal element alloys: a first-principles study

To cite this article: Libo Yu et al 2024 Phys. Scr. 99 065924

View the <u>article online</u> for updates and enhancements.

# You may also like

- The influence of nitrogen plasma on electrical and magnetic properties of epitaxial SrRuO<sub>3</sub> thin films
   Sicong Wei, Xing Ye, Shanquan Chen et al
- Topological phenomena at the oxide interfaces
   Kavya Ravindran, Jayjit Kumar Dey, Aryan Keshri et al.
- Topological Hall effect in SrRuO<sub>3</sub> thin films and heterostructures
   Xu Niu, Bin-Bin Chen, Ni Zhong et al.

# Physica Scripta



RECEIVED 15 March 2023

REVISED

28 March 2024

ACCEPTED FOR PUBLICATION
3 April 2024

PUBLISHED 6 May 2024

#### **PAPER**

Short-range-order degree dominated physical and mechanical properties of refractory multi-principal element alloys: a first-principles study

Libo Yu<sup>1</sup>, Jia Li<sup>1</sup>, Peter K Liaw<sup>2</sup> and Qihong Fang<sup>1</sup>

- State Key Laboratory of Advanced Design and Manufacturing Technology for Vehicle, College of Mechanical and Vehicle Engineering, Hunan University, Changsha, 410082, People's Republic of China
- <sup>2</sup> Department of Materials Science and Engineering, The University of Tennessee, Knoxville, TN 37996, United States of America

E-mail: fangqh1327@hnu.edu.cn

Keywords: refractory multi-principal element alloy, short-range order, first-principles calculation, physical property, mechanical property

#### Abstract

The degree of short-range order (SRO) can influence the physical and mechanical properties of refractory multi-principal element alloys (RMPEAs). Here, the effect of SRO degree on the atomic configuration and properties of the equiatomic TiTaZr RMPEA is investigated using the first-principles calculations. Their key roles on the lattice parameters, binding energy, elastic properties, electronic structure, and stacking fault energy (SFE) are analyzed. The results show the degree of SRO has a significant effect on the physical and mechanical properties of TiTaZr. During the SRO degree increasing in TiTaZr lattice, the low SRO degree exacerbates the lattice distortion and the high SRO degree reduces the lattice distortion. The high degree of SRO improves the binding energy and elastic stiffness of the TiTaZr. By analyzing the change in charge density, this change is caused by the atomic bias generated during the formation of the SRO, which leading to a change in charge-density thereby affecting the metal bond polarity and inter-atomic forces. The high SRO degree also reduces SFE, which means the capability of plastic deformation of the TiTaZr is enhanced.

## 1. Introduction

The refractory multi-principal element alloys (RMPEAs) have many advantages over traditional alloys [1], such as high strength and stability at high temperatures [2–6], which can be utilized to gas turbine engines in the aerospace industry [7–11]. In the past years, multi-principal element alloys (MPEAs) are traditionally assumed to be random solid solutions [12]. Recently, researches have revealed that the arrangement of atoms in MPEAs is not an ideal disordered state due to the diversity in the atomic radio, and the complex interactions between the constituent elements usually result in the chemical short-range order (SRO) structures [13–17]. The SRO is observed in the CoNiV RMPEA, and reduces the energy of the system [18]. The existence of SRO in the CuMn alloys promotes the planar slip, and thus leads to the anomalous recovery of the work hardening rate [19, 20]. Moreover, the L12 SRO is discovered in the CoCrNi RMPEA [20]. Notably, these SRO structures could improve the mechanical properties of MPEAs [21–25].

Although the exceptional mechanical properties have been found in RMPEAs, the origination of their mechanical properties is difficult to explore at the atomic level due to the diversity of the atomic environment in which they react at the atomic size and chemistry [26]. The first-principles calculations based on density functional theory (DFT) [27, 28] have the outstanding advantages in the atomic and electronic structures. For example, a recent study from DFT calculations has demonstrated that Ti, V, Zr, Nb, Mo, Hf, Ta, W and Re alloys exhibit local lattice distortions to some extent, and a severe local lattice distortion occurs only in the Zr- and/or Hf-containing RMPEAs [29]. Moreover, the elastic modulus calculated by DFT shows that doping with most alloying elements increases the strength of NbMoTaW RHEA, while only Zr-alloying increases the ductility [30]. To further explore the influence of SRO on the mechanical properties of RMPEAs, the lattice coefficients,

binding energy, elastic modulus, differential charge density, and stacking fault energy (SFE) are calculated using first-principles calculations in the present work. The contribution of SRO for the improvement of the mechanical properties of RMPEAs is evaluated in a multifaceted manner using these parameters. Here, the TiTaZr RMPEAs have superior mechanical properties [31, 32], which are selected as research objective. Hence, the physical and mechanical properties of the equiatomic TiTaZr RMPEA are investigated.

#### 2. Method and model

#### 2.1. First-principles calculation parameters

All first-principles calculations are performed by the VASP [33] based on the DFT. Here, the lattice coefficients, binding energy, elastic properties, electronic structure, and SFE are calculated. The adopted commutative-correlation functional is modified by Perdew–Burke–Ernzerhof (PBE) under the generalized gradient approximation [34]. Since the calculation involves thousands of structure energies in the DFT calculations, different calculation accuracies is adopted in the consideration of the cost when calculating different parameters. After the convergence test, the truncation energy of the plane-wave group is set to 300 eV, the density of K point is  $5 \times 5 \times 6$ , the energy-convergence standard is set to 0.01 meV, and the force convergence standard is  $10 \text{ meV} \text{ A}^{-1}$ , which are used to the calculation of the lattice coefficients, binding energy, electronic structure. For the elastic-modulus calculation, the density of the K point is change to  $3 \times 3 \times 3$ . For SFE calculation, the density of the K point is change to  $3 \times 3 \times 4$ .

#### 2.2. Short-range ordered parameter

The Warren-Cowley (WC) parameter is used to describe the degree of SRO, which is defined as [35, 36]:

$$\alpha_{ij} = \frac{p_{ij} - c_j}{\delta_{ij} - c_j} \tag{1}$$

where  $\alpha_{ij}$  is is the WC parameter for the i-j pair type in the first nearest neighbor shell,  $p_{ij}$  is the probability that an atom is a j-type atom in the first nearest neighbor shell of an i-type atom,  $c_j$  is the overall concentration of type j, and  $\delta_{ij}$  is the Kronecker delta. For the completely randomized alloys without SRO structure, the WC parameter is 0.

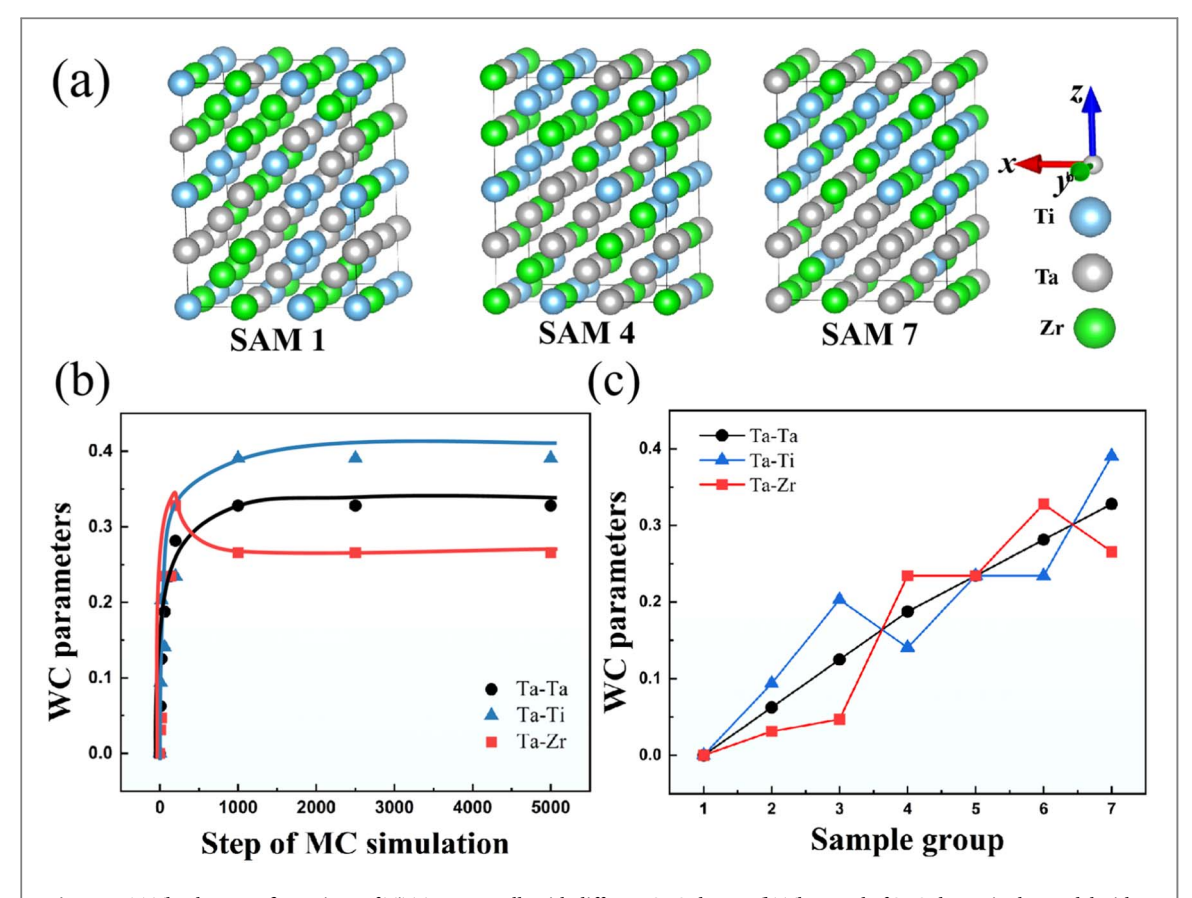
#### 2.3. Physical model

To study the SRO effect on the physical properties, the equiatomic TiTaZr bcc supercells for the configuration of  $2 \times 2 \times 2$  (16 atoms),  $3 \times 3 \times 4$  (72 atoms) and  $4 \times 4 \times 4$  (128 atoms) have been tested. Considering the accuracy and computational cost, the  $3 \times 3 \times 4$  supercell configuration is adopted. The initial model is a special quasirandom structure (SQS) [37], built by Alloy Theoretic Automated Toolkit (ATAT) software package [38]. Then, the initial model is iterated by Monte Carlo (MC) simulation [39] to form the SRO structures. According to the order of the number of iteration steps from 0 to 5000, seven samples are selected as research objects. Figure 1(a) shows the partial SRO structures, formed by MC simulation. Clearly, the aggregation of Ta atoms in the model becomes evident as the SRO degree increases. Here, the region where Ta atoms are polarized is considered as enhanced domain. The variation of SRO degree in the model is shown in table 1. Obviously, Ta-Ta, Ta-Ti and Ta-Zr groups show strong regularity. Figure 1(b) shows the variation of SRO degree in the model with increasing MC simulation steps, but stops increasing beyond 1000 steps. Figure 1(c) shows the trend of WC parameters of Ta-Ta, Ta-Ti and Ta-Zr groups for physical samples. From SAM 1 to SAM 7, the WC parameters show an overall increasing trend, which indicates the SRO degree increases from SAM 1 to SAM 7.

#### 2.4. Stacking fault energy model

Since building the SFE model on the basis of the physical models require intercepting the model obliquely according to the slip plane, which will lead to the degree of SRO in the intercepted region inconsistent with that of the physical models, thus affecting the accuracy of the results. So the SFE model needs to rebuild by SQS and MC simulation. In the bcc crystal, the  $\{110\}$  surface is the closest surface, which is easy to form dislocations. However, there is another possibility of forming dislocations on the  $\{112\}$  surface, which is the most common slip surface in a bcc crystal, providing favorable conditions for the formation of dislocations [40,41]. Therefore, all SFE models have  $\{112\}$  surface as their base, and the stacking surfaces are the  $\{112\}$  surface with a slip vector of 1/6  $\langle 111 \rangle$ . Figure 2(a) shows the schematic diagram of the bcc SFE model on the (112) surface along the [-1-11] direction. Figure 2(b) shows the SFE models with different SRO degree, which have 72 atoms. The truncation energy of the plane-wave group is set to 300 eV, the density of K point is  $5 \times 5 \times 6$ , the energy convergence standard is set to 0.01 meV, and the force convergence standard is 10 meV/A. Table 2 shows the

IOP Publishing



 $\textbf{Figure 1. (a)} \ The three configurations of \ TiTaZr \ supercells \ with \ different \ SRO \ degree. \textbf{(b)} \ The \ trend \ of \ SRO \ degree \ in \ the \ model \ with \ increasing \ MC \ simulation \ steps. \textbf{(c)} \ The \ trend \ of \ WC \ parameters \ for \ Ta-Ta, \ Ta-Ti \ and \ Ta-Zr \ in \ physical \ models.$ 

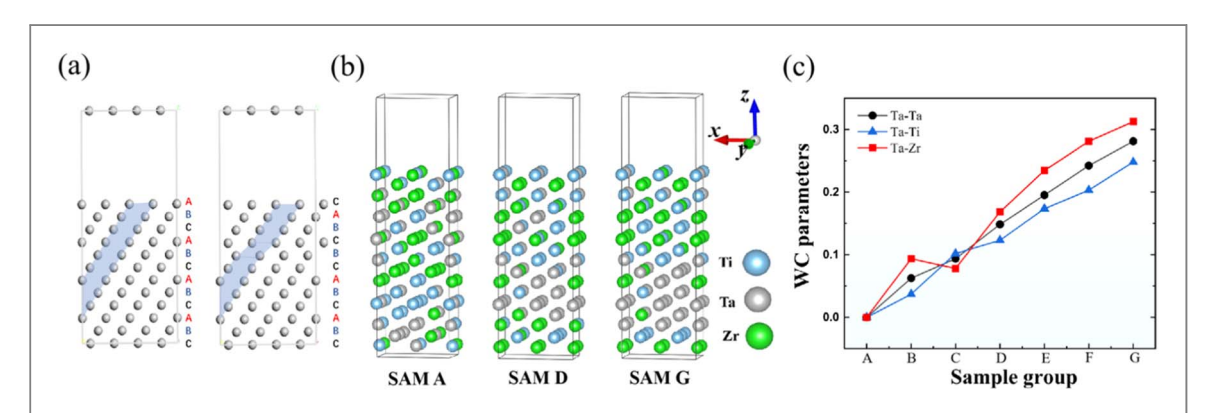


Figure 2. (a) Schematic diagram of the bcc SFE model on the (112) surface along the [-1-11] direction. (b) Representative possible configures of SFE model of TiTaZr with different degree of SRO. (c) The trend of WC parameters for Ta-Ta, Ta-Ti and Ta-Zr in SFE samples.

 $\textbf{Table 1.} \ The \ precise \ WC \ parameters \ of \ different \ TiTaZr \ physical \ models.$ 

Sample	$\alpha(Ta-Ta)$	$\alpha(Ta-Ti)$	$\alpha(Ta-Zr)$	$\alpha(Ti-Ti)$	$\alpha(Ti-Zr)$	$\alpha(Zr-Zr)$
SAM1	0	0	0	0	0	0
SAM2	0.0625	0.0938	0.0313	0.0469	0	0.0156
SAM3	0.1250	0.2031	0.0469	0.0156	-0.1719	-0.0625
SAM4	0.1875	0.1406	0.2344	-0.0938	-0.3281	-0.0469
SAM5	0.2344	0.2344	0.2344	-0.0625	-0.3594	-0.0625
SAM6	0.2813	0.2344	0.3281	-0.0625	-0.3594	-0.0156
SAM7	0.3280	0.3906	0.2656	0.0625	-0.2656	0

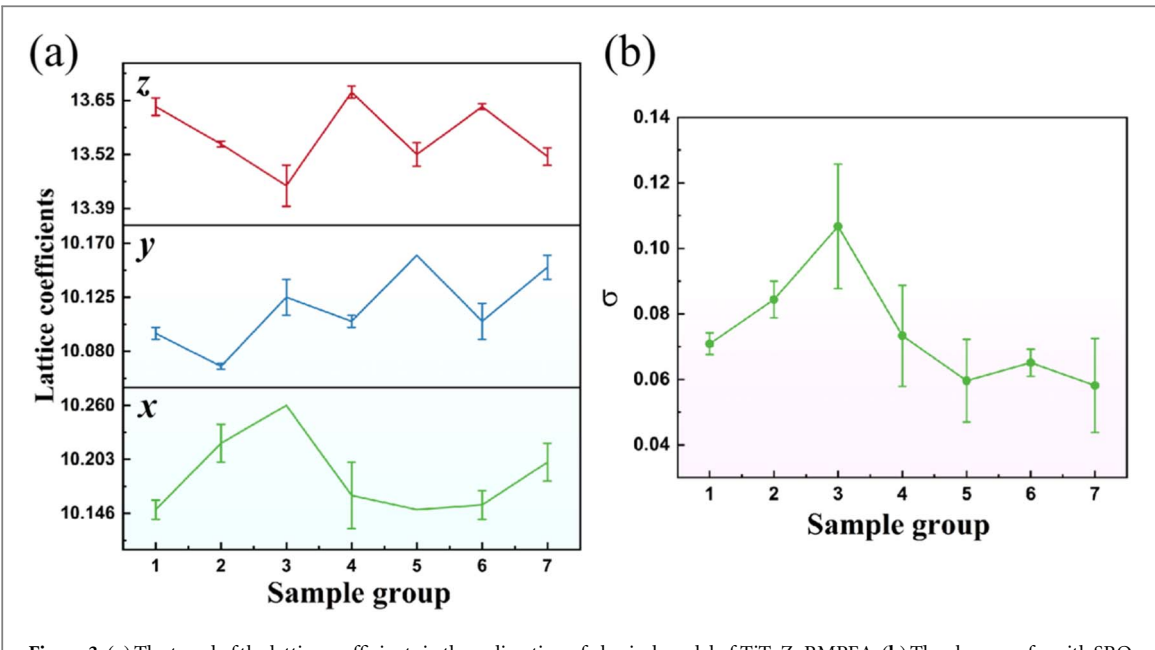


Figure 3. (a) The trend of the lattice coefficients in three direction of physical model of TiTaZr RMPEA. (b) The changes of  $\sigma$  with SRO degree.

Table 2. The precise WC parameters for the different TiTaZr SFE models.

Sample	$\alpha(Ta-Ta)$	$\alpha(Ta-Ti)$	$\alpha(Ta-Zr)$	$\alpha(Ti-Ti)$	$\alpha(Ti-Zr)$	$\alpha(Zr-Zr)$
SAM A	0	0	0	0	0	0
SAM B	0.0625	0.0369	0.0938	0.0156	-0.0625	-0.0156
SAM C	0.0938	0.1019	0.0781	-0.0234	-0.1653	-0.0469
SAM D	0.1484	0.1231	0.1685	-0.0234	-0.2344	-0.0313
SAM E	0.1953	0.1735	0.2344	-0.0469	-0.2519	0
SAM F	0.2422	0.2031	0.2812	-0.0625	-0.3204	-0.0234
SAM G	0.2813	0.2418	0.3125	-0.0469	-0.3204	-0.0078

WC parameters for these configurations. Figure 2(c) shows the trend of WC parameters of Ta-Ta, Ta-Ti and Ta-Zr groups for SFE samples.

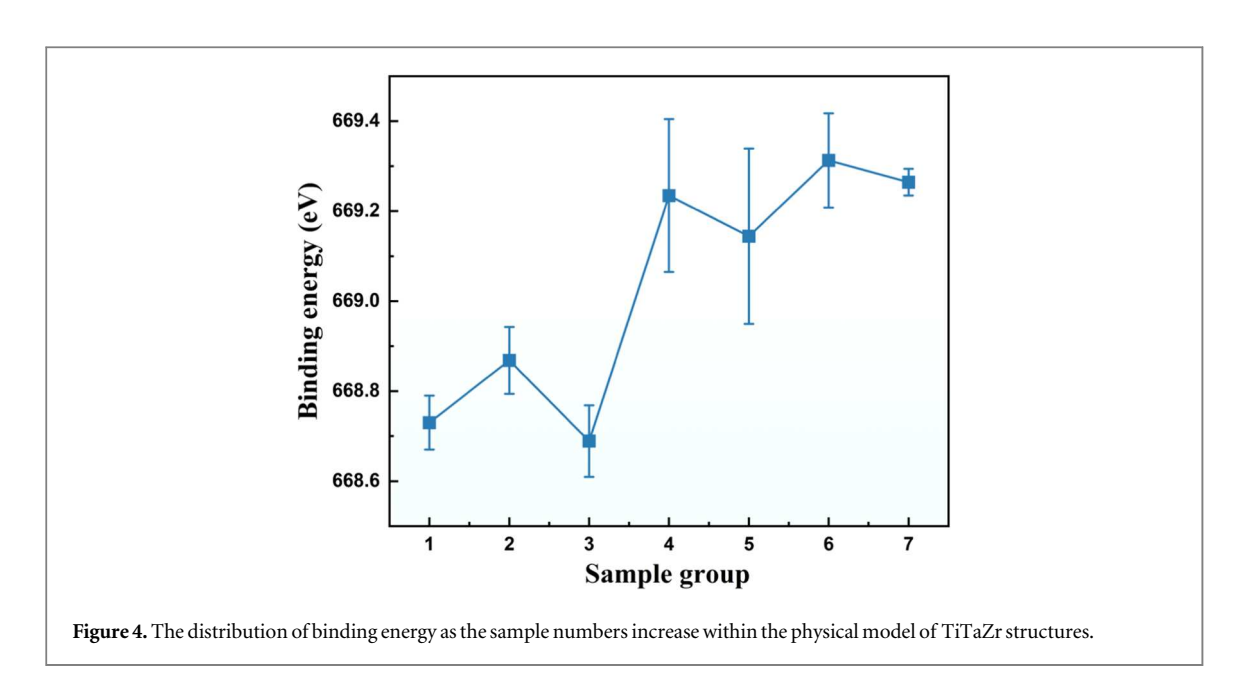
#### 3. Results and discussion

In order to avoid errors from randomness, three sets of different configurations with the same WC parameters are calculated for the lattice coefficients, binding energy, elastic modulus and SFE, and all the results are represented in the form of error bars. All models are structurally optimized in order for the results to be closed to reality.

Figure 3(a) presents the trendss of lattice coefficient in x, y and z-direction of physical sample groups after structural optimization by DFT. In order to visualize the lattice variations of the physical model more intuitively, the standard deviation of lattice coefficient  $\sigma$  is used here:

$$\sigma = \sqrt{\frac{(l_x - \bar{l}_x)^2 + (l_y - \bar{l}_y)^2 + (l_z - \bar{l}_z)^2}{3}}$$
 (2)

where  $l_x$ ,  $l_y$  and  $l_z$  are the lattice coefficients of x, y and z-direction after structural optimization.  $\bar{l}_x$ ,  $\bar{l}_y$  and  $\bar{l}_z$  is the lattice coefficient of x, y and z-direction of initial model at the energy minimum obtained by DFT static calculations. Therefore, the standard deviation  $\sigma$  can indicate the deviation degree of the relaxed model from the stable initial lattice model. Figure 3(b) shows the trend of  $\sigma$ , the value of  $\sigma$  initially increase from SAM 1 to SAM 3, which is consistent with the trend of the WC parameter. However, it decreases sharply from SAM 3 to SAM 4 and keep low value form SAM 4 to SAM 7. The change of  $\sigma$  implies that the lattice distortion is becoming severe at first, but starts to weaken when the SRO structure is strong enough. Thus low degree SRO promotes lattice distortion and high degree SRO favors lattice stabilization. Comparing the trends of WC parameter of Ta-Ta,



Ta-Ti and Ta-Zr, the change of Ta-Ta and Ta-Ti are smaller from SAM 3 to SAM 4, but the Ta-Zr shows a large change (figure 1(c)). It implies that the SRO degree of Ta-Zr may have a greater effect on the physical properties of TiTaZr.

Figure 4 exhibits the effect of SRO degree on the binding energy in physical models. The binding energy is smaller and less variable from SAM 1 to SAM 3. However, there is a large increase in the binding energy from SAM 3 to SAM 4 and keep high value from SAM 4 to SAM 7. This change node is the same as the  $\sigma$ , which again coinciding with the later results. It suggests that the SRO structure with high degree will lead to a more stable lattice. The trend of binding energy is similar to the WC parameters of Ta-Zr (the blue points in figure 1(c)), which indicates SRO degree of Ta-Zr have a greater effect. This also proves that there is a stronger interaction between atoms in the process of SRO enhancement.

Figure 5 presents the relationship between the SRO degree and elastic properties of physical models, which is calculated by the Voigt-Reuss-Hill [42] method after processing the elastic-stiffness matrix by DFT. The Voigt average formula is described as follows:

$$G = \frac{1}{5}[(C_{11} - C_{12}) + 3C_{44}] \tag{3}$$

$$B = \frac{1}{3}(C_{11} + 2C_{12}) \tag{4}$$

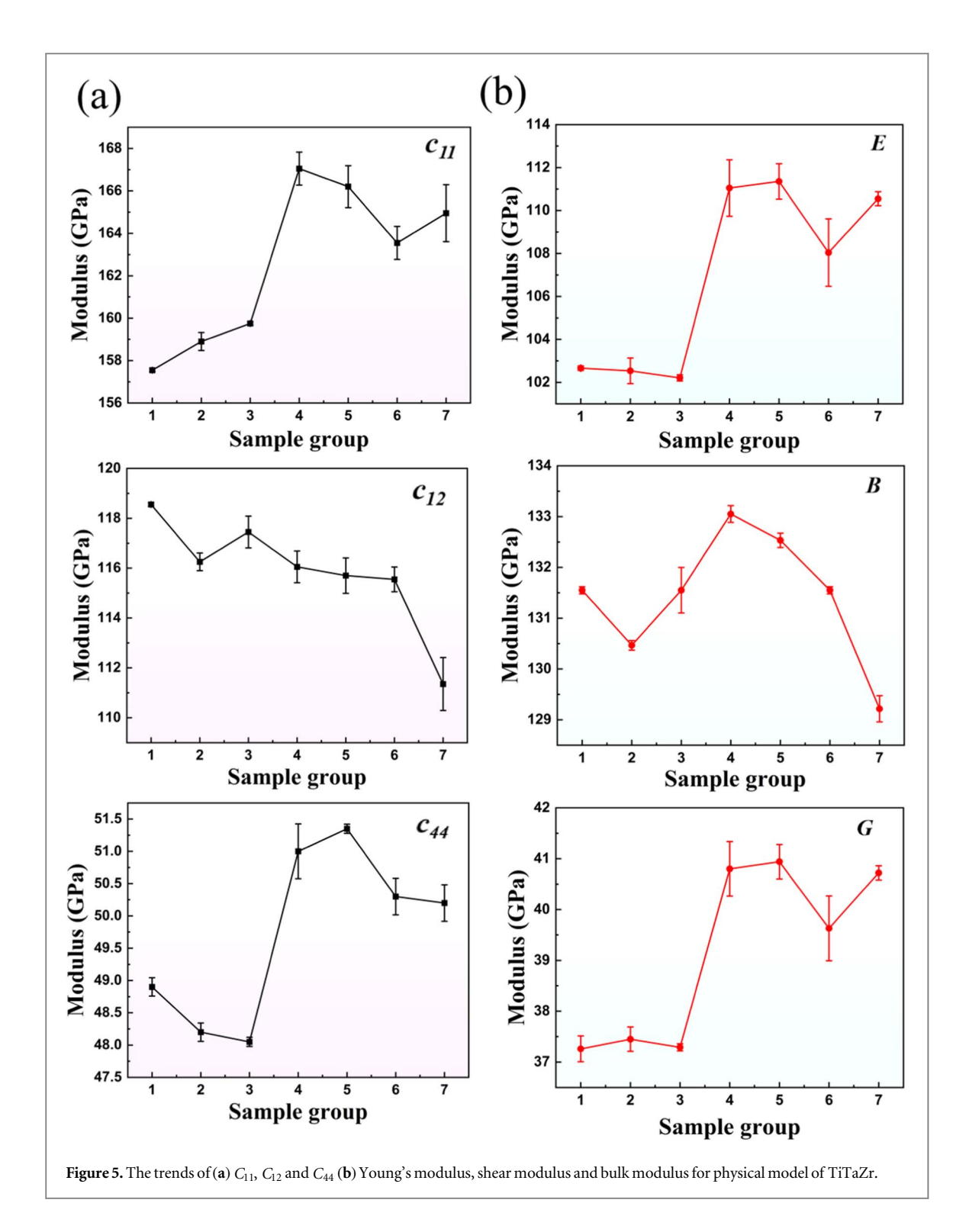
$$E = \frac{9BG}{3B + G} \tag{5}$$

where  $C_{11}$ ,  $C_{12}$  and  $C_{44}$  is elastic constant in stiffness matrix and, in particular, the cubic crystal system has only three independent matrix elements. E is the Young's modulus, G is the shear modulus, and B is the bulk modulus [43]. Figure 5(a) shows the trends of  $C_{11}$ ,  $C_{12}$  and  $C_{44}$ , where  $C_{11}$  and  $C_{44}$  increase sharply from SAM 3 to SAM 4 and  $C_{12}$  shows an overall decreasing trend. Figure 5(b) shows the trends of E, B and G. Obviously, E and G have a dramatic increase from SAM 3 to SAM 4. According to equations (4)–(6), this trend is due to the change of  $C_{11}$  and  $C_{44}$ , since the larger value of  $C_{11}$  so it contributes the most. This results indicate the elastic stiffness of the material becomes stronger and the bonding between the metal atoms becomes stronger, which is consistent with the binding energy result. The change point is similar to the lattice coefficient and the binding energy, and can be taken as evidence that testifying to a high degree of SRO has a significant effect, especially Ta-Zr.

The charge-density difference is used to visualize the flow of electrons after the interaction of individual fragments or the change of the electron density during the formation of atoms into molecules. At present, there are three expressions for the charge-density difference, one of which was chosen for this calculation and is calculated as follows:

$$\Delta \rho = \rho_{AB} - \rho_A - \rho_B \tag{6}$$

where  $\rho_{AB}$  is the charge density of the whole system,  $\rho_A$  is the charge density of the fragment composed of a Taatomic distribution, and  $\rho_B$  is the charge density of the fragment composed of Ti and Zr atomic distributions [44]. Here, the SAM 1, SAM 4, and SAM 7 are chosen as the representative samples. In order to visualize this effect more substantially, a plane-averaged charge-density difference diagram is introduced to reflect the charge-



flow direction [45]. Here, it is obtained by dividing the model into 160 planes along *z*-direction and then calculating the charge-density difference for each plane. Figure 6(a) shows the difference plane of planar cloud maps in physical models and statistics direction of the plane-averaged charge-density difference diagram. Figure 6(b) shows the planar cloud maps of the charge-density difference in difference plane, which obtained by DFT calculation followed by VESTA processing. Here, the color indicate the value of charge-density difference. Figure 6(c) plots the plane-averaged charge-density difference diagrams. Combining the planar cloud maps and plane-averaged diagrams, it can be clearly observed that the enhanced-SRO domains (left side of the model) loses much charge while the right side gains charge. This represents a change in the polarity of the metal bond and increased strength of metal bonds. This result suggests that the Ta atom bias caused by the high degree SRO makes the binding of Ta atoms to other atoms stronger. This is the reason of the enhancement in binding energy and elastic.

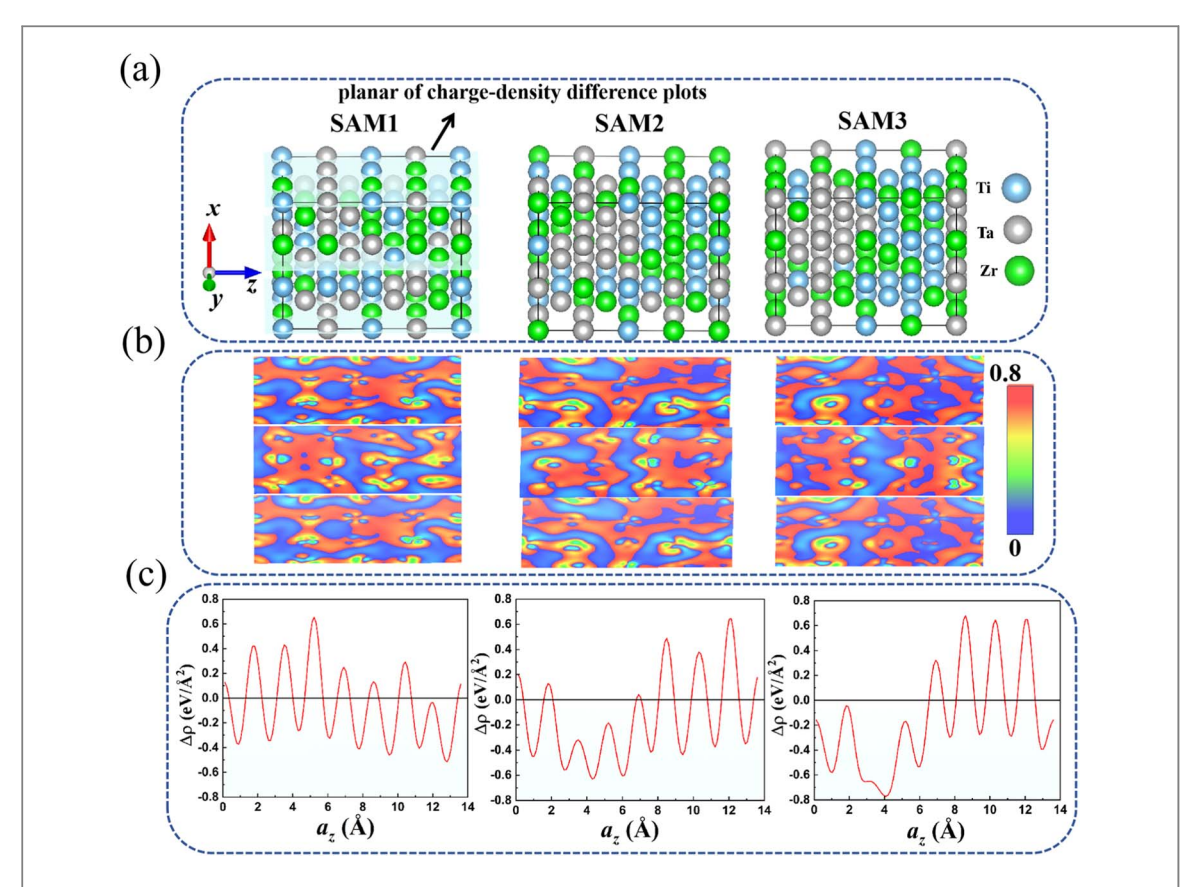
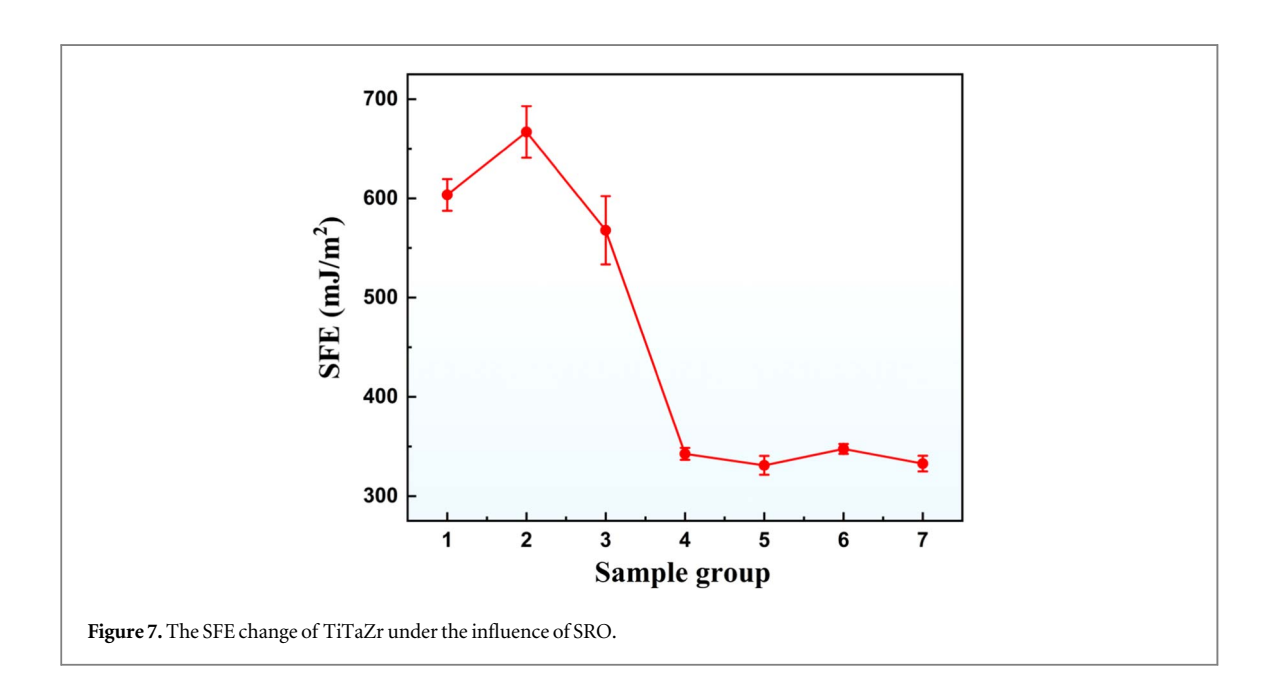
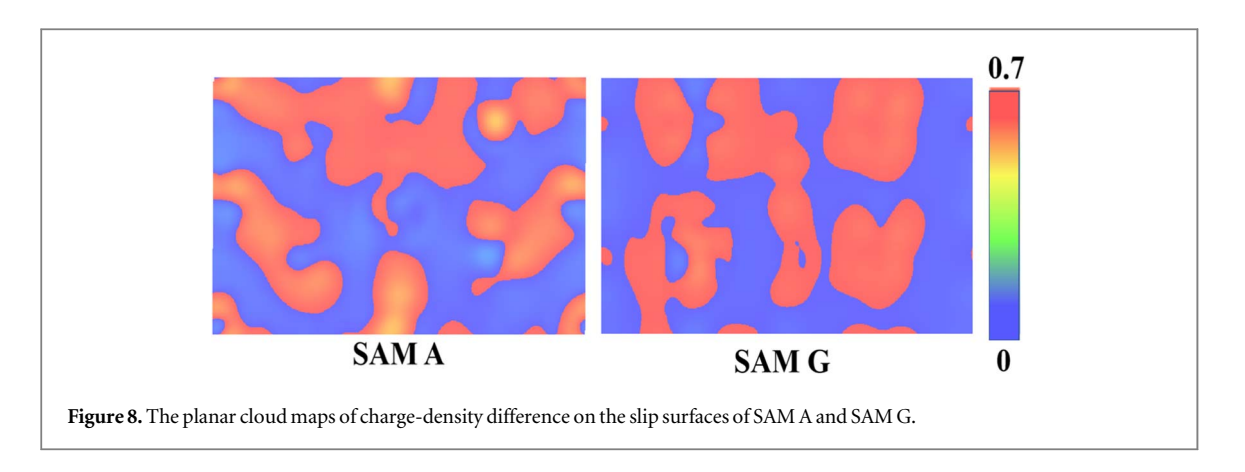


**Figure 6.** (a) The position of the difference plane of planar cloud maps in physical models and statistics direction of the plane-averaged charge-density difference diagram. (b) The planar-cloud plot for three typical TiTaZr lattice samples. (c) The plane-averaged charge-density difference for three typical TiTaZr lattice samples.



The SFE measures the energy cost for shearing one atomic plane with respect to another, which is directly connected to the response of plasticity deformation. SFE is usuall used to connect results from atomistic simulation to macroscopic properties. When the SFE decreases, crystalline material can deform by either dislocation slip, transformation-induced plasticity, or twinning induced plasticity [46, 47]. Figure 7 shows the effect of SRO degree on the SFE. Clearly, from SAM A to SAM C the value of SFE is around 600. From SAM D to SAM G, the SFE decreases considerably and remains around 350. Similarly, the position that SFE significantly reduced is consistent with the calculations of physical parameters. However, in the SFE model, the WC parameter of Ta-Zr does not increase so large from SAM C to SAM D, so the decrease of SFE is mainly due to the



co-effect of the increasing SRO degree of Ta-Ta, Ta-Ti and Ta-Zr. This means the high SRO degree is beneficial for slip dislocations and can enhance plastic deformation.

Figure 8 shows the planar cloud maps of charge-density difference on the slip dislocation plane of SAM A and SAM G. Compared to SAM A with a low SRO degree, the SAM G with a high SRO degree has a darker red color in the charge-density differential region in the charge-density difference cloud map. It is implies a higher density of charge-difference on the slip dislocation planes of SAM G.

The above results indicate that low degree of SRO has limited effect on TiTaZr, while high degree of SRO can dominate the physical and mechanical properties changes of TiTaZr RMPEA. In physical model, the SRO degree of Ta-Zr significantly affects the physical properties. In SFE model, the influence of Ta-Zr become mild, but the co-effect of increasing SRO degree of Ta-Ta, Ta-Ti and Ta-Zr also results in a large decrease in SFE. From SAM 1 to SAM 3 and SAM A to SAMC, the distribution of atoms in the model is dispersed and has not yet formed the enhanced-SRO domain. From SAM 3 to SAM 7 and SAM D to SAM G, the discrete Ta atoms start to aggregate highly (figures 1 and 2). When the enhanced-SRO domains is formed, significant charge flow occurs between the enhanced-SRO domain and another, as shown in figures 6 and 8. Because changes in charge-density affect metal bond polarity and inter-atomic forces, this paper considers the effect of charge flows due to the polarization of Ta atoms is an important reason for the effect of SRO strengthening on physical properties. Moreover, this effect is good for the strength and toughness of TiTaZr RMPEA.

### 4. Conclusion

In summary, the effect of SRO degree on the physical and mechanical properties in a TiTaZr RMPEA is studied using first-principles calculations. The lattice coefficients, binding energy and elastic properties of the crystal change drastically with the high SRO. This implies high SRO degree results in better elastic stiffness and stability. Observing changes in charge-structure, there are significant loss of charge in the enhanced-SRO domains. This means the stronger interaction between atoms in enhanced-SRO domain. Ta atom bias caused by the high degree SRO makes the binding of Ta atoms to other atoms stronger. Similarly, the SFE keep a low value at high SRO degree, and a high value at low SRO degree. This implies high SRO degree results in better plastic deformation. The aggregation of atoms in the process of increasing SRO degree leads to a loss of charges, which influences the metal-bond polarity and affects the physical and mechanical properties of the RMPEAs. This work reveal the impact of SRO on RMPEAs and the sources of that impact. In conclusion we suggest that if the mechanical properties need to be enhanced by adjusting the SRO, a higher degree of SRO is required and this high degree is reflected in the bias of the atoms.

#### Acknowledgments

The authors would like to deeply appreciate the supports from National Natural Science Foundation of China (12372069, and 12172123), Natural Science Foundation of Hunan Province (2022JJ20001), and the Hunan Provincial Innovation Foundation for Postgraduate (CX20220378). PKL very much appreciates the support from the National Science Foundation (DMR-1611180, 1809640, and 2226508).

#### Data availability statement

All data that support the findings of this study are included within the article (and any supplementary files).

#### **Declarations conflict of interests**

The authors declare that they have no conflict of interest.

#### **ORCID** iDs

Jia Li https://orcid.org/0000-0003-4739-381X

#### References

- [1] George E P, Curtin W A and Tasan C C 2020 High entropy alloys: a focused review of mechanical properties and deformation mechanisms *Acta Mater.* **188** 435–74
- [2] Lee C et al 2021 Strength can be controlled by edge dislocations in refractory high-entropy alloys Nat. Commun. 12 5474
- [3] Frey C, Silverstein R and Pollock T M 2022 A high stability B2-containing refractory multi-principal element alloy *Acta Mater.* 229 117767
- [4] Qin G et al 2021 Experimental and theoretical investigations on the phase stability and mechanical properties of Cr7Mn25Co9Ni23Cu36 high-entropy alloy Acta Mater. 208 116763
- [5] Ma E and Wu X 2019 Tailoring heterogeneities in high-entropy alloys to promote strength-ductility synergy, Nat. Commun. 10 5623
- [6] Guan Z, Feng C, Song H, Zhang Y and Zhang F 2022 Effects of Ge addition on the structure, mechanical and magnetic properties of (CoCrFeNi) 100-xGex high-entropy alloys Phys. Scr. 97 125701
- [7] Arif Z U, Khalid M Y and Rehman E 2022 Laser-aided additive manufacturing of high entropy alloys: processes, properties, and emerging applications J. Manuf. Proc. 78 131–71
- [8] Li Z et al 2022 Design of TiZrNbTa multi-principal element alloys with outstanding mechanical properties and wear resistance Mater. Sci. Eng. A 845 143203
- [9] Senkov O N, Senkova S V, Miracle D B and Woodward C 2013 Mechanical properties of low-density, refractory multi-principal element alloys of the Cr–Nb–Ti–V–Zr system Mater. Sci. Eng. A 565 51–62
- [10] Li Z, Zhao S, Ritchie R O and Meyers M A 2019 Mechanical properties of high-entropy alloys with emphasis on face-centered cubic alloys Pro. Mater. Sci. 102 296–345
- [11] Wang M et al 2021 A novel bulk eutectic high-entropy alloy with outstanding as-cast specific yield strengths at elevated temperatures Scr. Mater. 204 114132
- [12] Niu J et al 2014 In situ observation of random solid solution zone in LiFePO4 electrode Nano Lett. 14 4005-10
- [13] Santodonato L J et al 2015 Deviation from high-entropy configurations in the atomic distributions of a multi-principal-element alloy Nat. Commun. 6 5964
- [14] Zhang FX et al 2017 Local structure and short-range order in a NiCoCr solid solution alloy Phys. Rev. Lett. 118 205501
- [15] Schönfeld B et al 2019 Local order in Cr-Fe-Co-Ni: Experiment and electronic structure calculations Phys. Rev. B 99 014206
- [16] Wang S D et al 2021 Chemical short-range ordering and its strengthening effect in refractory high-entropy alloys Phys. Rev. B 103 104107
- $[17] \ \ Bu\ Y\ Q\ and\ Wang\ H\ T\ 2021\ Short-range\ order\ in\ multicomponent\ alloys\ \textit{Adv.\ Mech.}\ 51\ 915-9$
- [18] Chen X et al 2021 Direct observation of chemical short-range order in a medium-entropy alloy Nature 592 712-6
- [19] Han D et al 2019 Anomalous recovery of work hardening rate in Cu-Mn alloys with high stacking fault energies under uniaxial compression Mater. Sci. Eng. A 743 745–54
- $[20]\ \ N\"{o}hring\ W\ G\ and\ Curtin\ W\ A\ 2018\ Cross-slip\ of long\ dislocations\ in\ FCC\ solid\ solutions\ Acta\ Mater.\ 158\ 95-117$
- [21] Hsiao H W et al 2022 Data-driven electron-diffraction approach reveals local short-range ordering in CrCoNi with ordering effects Nat. Commun. 13 6651
- [22] Zhang R et al 2020 Short-range order and its impact on the CrCoNi medium-entropy alloy Nature 581 283-7
- [23] Xing B, Wang X, Bowman W J and Cao P 2022 Short-range order localizing diffusion in multi-principal element alloys Scr. Mater. 210
- [24] Liu SF et al 2018 Stacking fault energy of face-centered-cubic high entropy alloys Intermetallics 93 269-73
- [25] Chen S et al 2021 Simultaneously enhancing the ultimate strength and ductility of high-entropy alloys via short-range ordering Nat. Commun. 12 4953
- [26] Kube S A et al 2019 Phase selection motifs in High Entropy Alloys revealed through combinatorial methods: Large atomic size difference favors BCC over FCC Acta Mater. 166 677–86
- [27] Kohn W and Sham L 1996 Density functional theory Conf. Proc. Phys. Soc 49 561-572
- [28] Mazin I, Johannes M, Boeri L, Koepernik K and Singh DJ 2008 Problems with reconciling density functional theory calculations with experiment in ferropnictides Phys. Rev. B 78 085104
- [29] Tong Y et al 2020 Severe local lattice distortion in Zr-and/or Hf-containing refractory multi-principal element alloys Acta Mater. 183 172–81
- [30] Tong Y et al 2020 Influence of alloying elements on mechanical and electronic properties of NbMoTaWX (X = Cr, Zr, V, Hf and Re) refractory high entropy alloys Intermetallics 126 106928
- [31] Whitfield T E et al 2020 Elucidating the microstructural development of refractory metal high entropy superalloys via the Ti–Ta–Zr constituent system, J. Alloy. Comp. 818 152935
- [32] Nagase T et al 2020 Design and fabrication of Ti–Zr-Hf-Cr-Mo and Ti–Zr-Hf-Co-Cr-Mo high-entropy alloys as metallic biomaterials, Mater. Sci. Eng. C 107 110322
- [33] Hafner J 2008 Ab-initio simulations of materials using VASP: Density-functional theory and beyond, J. Comput. Chemistry 29 2044–78
- [34] Perdew JP, Burke K and Ernzerhof M 1996 Generalized gradient approximation made simple Phys. Rev. Lett. 77 3865
- [35] Cowley J M 1950 An approximate theory of order in alloys Phys. Rev. 77 669
- [36] Cowley J M 1960 Short-and long-range order parameters in disordered solid solutions *Phys. Rev.* 120 1648
- [37] Zunger A, Wei S-H, Ferreira L and Bernard J E 1990 Special quasirandom structures *Phys. Rev. Lett.* 65 353
- [38] Van De Walle A, Asta M and Ceder G 2002 The alloy theoretic automated toolkit: a user guide Calphad 26 539-53

[39] Zhang R, Zhao S, Ding J, Chong Y, Jia T, Ophus C, Asta M, Ritchie R O and Minor A M 2020 Short-range order and its impact on the CrCoNi medium-entropy alloy *Nature* 581 283–7

- [40] Zhang X C et al 2023 Unstable stacking fault energy and peierls stress for evaluating slip system competition in body-centered cubic metals J. Mater. Res. Tech. 22 3413–22
- [41] Queyreau S et al 2011 Edge dislocation mobilities in bcc Fe obtained by molecular dynamics Phys. Rev. B 84 064106
- [42] Ikehata H et al 2004 First-principles calculations for development of low elastic modulus Ti alloys Phy. Rev. B 70 174113
- [43] Xie M Y and Li F X 2022 Review of the measurement methods for elastic moduli and internal friction of solids Adv. Mech. 52 33–52
- [44] Hu Y L et al 2022 First-principle calculation investigation of NbMoTaW based refractory high entropy alloys J. Alloy. Comp. 827 153963
- [45] Dai J H, Song Y and Yang R 2017 Influence of alloying elements on stability and adhesion ability of TiAl/TiO2 interface by first-principles calculations *Intermetallics* 85 80–9
- [46] Li Z, Pradeep K G, Deng Y, Raabe D and Tasan C C 2016 Metastable high-entropy dual-phase alloys overcome the strength–ductility trade-off Nature 534 227-30
- [47] Grässel O, Krüger L, Frommeyer G and Meyer L 2000 High strength Fe–Mn–(Al, Si) TRIP/TWIP steels development—properties—application Inter. J. Plast. 16 1391–409